Ultraefficient Förster-Type Nonradiative Energy Transfer Enabled by the Complex Dielectric Medium with Tuned Permittivity

Pedro Ludwig Hernandez-Martinez, Abdulkadir C. Yucel,* and Hilmi Volkan Demir*

Cite This: *J. Phys. Chem. C* 2021, 125, 12405−12413

Read Online

ACCESS | Metrics & More | Article Recommendations | SI Supporting Information

ABSTRACT: Förster-type nonradiative energy transfer (FRET) is one of the primary near-field phenomena and is a useful, fundamental mechanism allowing us to control the excitation energy flow. Using carefully chosen pairs of quantum emitters/absorbers (donors/acceptors), FRET has proved to be essential in a variety of light-generating and -harvesting systems. However, FRET takes place only in a limited spatial range, and its efficiency suffers from an adversely rapidly decreasing profile over the increasing distance between the donor and acceptor. To foster FRET, reaching ultimate levels of efficiency and extending its range, we systematically studied the FRET mechanism by tuning the background medium's permittivity. The FRET rates of donor−acceptor pairs consisting of a point-like, quasi-0-dimensional quantum dot and quasi-2-dimensional quantum well nanostructures are analytically derived to characterize the change of FRET rates with respect to the medium's permittivity. The analysis reveals that the FRET rate becomes singular when the permittivity approaches zero and there is a fixed value for the point-like and all other nanostructures, respectively. By setting the medium's relative permittivity to realistic values near the singular point, which can be realized by a digital metamaterial approach, ultrahigh FRET rates and thereby ultraefficient FRET-based systems are achievable.
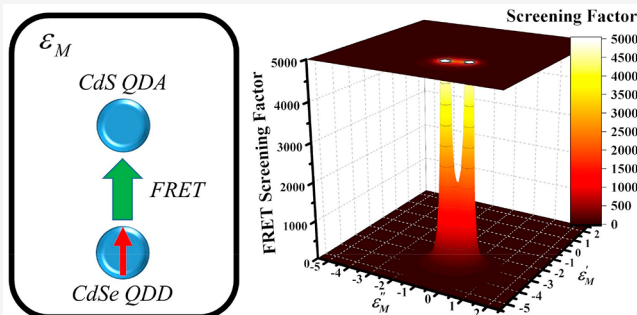
I. INTRODUCTION

Förster-type nonradiative energy transfer (FRET) is a directional process, allowing for the transfer of the excitons from donor particles to acceptor particles, enabled by nonradiative dipole−dipole interactions between them. FRET exploits the proximity effect that strongly depends on (i) the center-to-center distance between the donor and acceptor and (ii) its Förster radius as a pair.[1] Due to the strong distance dependence of the dipole−dipole coupling, efficient FRET is only achievable in a limited length scale, typically approximately 10 nm. To this end, several techniques were developed to increase the FRET efficiency and range in the past. In refs 2−4, FRET distance dependency is alleviated by changing the nanocrystal geometry, for example, from a quantum dot (QD) to a quantum well (QW), which consequently increases the FRET rate.[5] However, this improvement remains limited. In refs 6−9, the strength of the donor−acceptor coupling is increased by using local electric field enhancement, resulting in the acceleration of the FRET rate. This local electric field enhancement is achieved by the use of localized surface plasmon near metal nanoparticles. However, due to the lossy properties of metal nanoparticles, placing metal nanoparticles to enhance the exciton transfer rate can result in a decrease in the FRET rate if not carefully designed.

Recently, the epsilon-near-zero (ENZ) materials, i.e., materials with near-zero permittivity, have also received significant attention. These materials exhibit many interesting phenomena, including decoupling of the electric and magnetic field at a nonzero frequency and strong light−matter interactions, which can be used to study different wave dynamics.[10,11] These effects are accompanied by enlargement of the operating wavelength and decoupling of the spatial and temporal field variations. Consequently, the electric and magnetic fields' phase distribution is nearly constant in such an ENZ medium. These peculiar phenomena have been exploited to obtain highly directive beams,[12] perform beamforming and beam-steering tasks,[13] enhance nonlinear response,[14] and guide electromagnetic energy through channels of arbitrary geometry.[11] Moreover, the phase uniformity in ENZ materials has also been used to enhance the Purcell factor[15−17] of single quantum emitters. However, no previous study has investigated the effects of ENZ medium's tuned permittivity and the resulting unique features on substantially accelerating the FRET rate and hence pushing the limits of the FRET range.

In this work, we aim to fill this gap and show the critical effects of a dielectric background medium with carefully tuned complex permittivity on the superior enhancement of the donor−
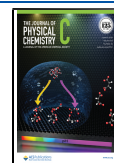
acceptor coupling and demonstrate a distinct set of generic conditions to be imposed on the dielectric environment to reach ultimate levels of efficiency in an extended space. Such an ultimate enhancement in the Förster process leads to a significant enlargement of the Förster radius. To quantify such enhancement, we derived the analytical expressions for the FRET rates of donor–acceptor pairs consisting of point-like, QD, and QW nanostructures. Next, this analytical formulation is rigorously used to identify the background permittivity conditions that yield the maximized FRET rates. Our analysis results show that the point-like pairs exhibit the maximum FRET rate when the relative permittivity approaches zero (i.e., when the background medium is an ENZ medium). On the other hand, different from the case of point-like FRET pairs, the FRET rates of QD and QW donor–acceptor pairs reach, surprisingly, their maxima at modified permittivity values, shifted away from the zero. These fixed permittivity values depend on the QD and QW's relative permittivities; this is determined via the screening effect factors indicated in the derived analytical expressions. The FRET singularity happens when the screening effect factor's denominator approaches zero, resembling the plasmonic effect.

Our numerical tests show that an ultrahigh FRET rate is achievable using tuned permittivity of background dielectric medium. For example, when the CdSe QD donor and acceptor are embedded in a medium with the relative complex permittivity of -2 + i, which can be fabricated using, for example, Ag and SiN layers,[18] the FRET rate is enhanced by 53 times compared to that of the same nanostructures in the vacuum. Likewise, when the CdSe QW donor and CdSe QD acceptor are placed in a medium with relative permittivity -2 + i, the enhancement is more than 3-folds. On the contrary, when CdSe QD donor and CdSe QW acceptor are enclosed in the same medium, the enhancement factor exceeds 32. Finally, in the case of the CdSe QW donor–acceptor pair embedded in a medium with relative permittivity -2 + i, the FRET rate can be boosted more than 2. These findings show that the FRET rate can be increased drastically by carefully selecting the donor–acceptor pair's geometry along with the permittivity of the background medium. This boost in the FRET rate will benefit numerous applications, including color tuning, sensing, light harvesting, and light generation.

The rest of the paper is organized as follows. Section II presents the analytical expressions to compute the FRET rates and FRET screening effect factors for the following cases: (1) point-like (D)/rectangular-like (QW) donor and point-like acceptor (A) case, referred to as the D/QWD-A case, (2) spherical-like (QD) donor and point-like acceptor case, referred to as the QDD-A case, (3) point-like/rectangular-like donor and rectangular-like acceptor case, referred to as the D/QWD-QWA case, (4) point-like/rectangular-like donor and spherical-like acceptor case, referred to as the D/QWD-QDA case, (5) spherical-like donor and spherical-like acceptor case, referred to as the QDD-QDA case, and (6) spherical-like donor and rectangular-like acceptor case referred to as the QDD-QWA case. Furthermore, for each case, the section provides the validation of the analytical expressions via numerical simulations. The section is finalized by comparing the FRET enhancement factor for the cases of CdSe donor–acceptor pair configurations, including (1) QDD-QDA, (2) QWD-QDA, (3) QDD-QWA, and (4) QWD-QWA. The effect of the donor–acceptor pair configurations on the FRET rate is discussed. Section III summarizes our findings and conclusions.

II. RESULTS AND DISCUSSION

In general, the FRET rate γ_{trans} is the average over the FRET rates of the x-, y-, and z-excitons, where

$$\gamma_{\text{trans}} = \frac{\gamma_{x,\text{trans}} + \gamma_{y,\text{trans}} + \gamma_{z,\text{trans}}}{3} \tag{1}$$

Here $\gamma_{\alpha,\text{trans}}$ is the probability for an α-exciton, $\alpha = \{x,y,z\}$, to be transferred from a donor to an acceptor, computed via refs 2, 3, and 6 in CGS units

$$\gamma_{\alpha,\text{trans}} = \frac{2}{\hbar} \text{Im}\left[\int dV \left(\frac{\varepsilon_A(\omega)}{4\pi}\right) \mathbf{E}_\alpha(\mathbf{r}) \cdot \mathbf{E}_\alpha^*(\mathbf{r})\right] \tag{2}$$

In this expression, the integration is carried out over the acceptor's volume. Here, $\varepsilon_A(\omega)$ is the frequency-dependent permittivity of the acceptor, and $\hbar$ is the Planck's constant. $\mathbf{E}_\alpha(\mathbf{r}) = -\nabla\Phi_\alpha(\mathbf{r})$ is the electric field inside the acceptor due to an α-exciton at the donor under the electrostatic conditions. The electric potential generated by the α-exciton, $\Phi_\alpha(\mathbf{r})$, is given by

$$\Phi_\alpha(\mathbf{r}) = \left(\frac{ed_{\text{exc}}}{\varepsilon_{\text{eff}}}\right)\frac{(\overline{\mathbf{r}} - \overline{\mathbf{r}}_0)\cdot\hat{\boldsymbol{\alpha}}}{|\mathbf{r} - \mathbf{r}_0|^2} \tag{3}$$

where $\mathbf{r}_0$ and ed_{exc} are the position vector and dipole moment of the exciton, respectively, and $\mathbf{r}$ is the observation point. ε_{eff} denotes the donor's effective relative permittivity, which depends on the geometry of the nanostructure and the dipole orientation of exciton $\alpha = \{x,y,z\}$. In what follows, we make use of CGS units; thus, e is given in esu units; d_{exc}, $\mathbf{r}_0$, and $\mathbf{r}$ are in centimeters; and $\varepsilon_{\{\text{eff},D,A,M\}} = \varepsilon'_{\{\text{eff},D,A,M\}} + i\varepsilon''_{\{\text{eff},D,A,M\}}$ is the complex relative permittivity of the effective, donor, acceptor, and medium, respectively, where $\varepsilon'_{\{\text{eff},D,A,M\}}$ is the real and $\varepsilon''_{\{\text{eff},D,A,M\}}$ is the imaginary part. Although $\varepsilon_{\{\text{eff},D,A,M\}}$ is a function of both the position and frequency, we assume that it depends only on the frequency unless stated otherwise. For point-like and planar geometries, ε_{eff} equals to ε_M, and for spherical geometry, ε_{eff} equals to $(\varepsilon_D + 2\varepsilon_M)/3$,[3] where ε_D is the relative permittivity of the spherical particle (QD) serving as a donor. Here, we based our formalism on these geometries; therefore, the corresponding electric potential for the point-like and planar geometries is

$$\Phi_\alpha(\mathbf{r}) = \left(\frac{ed_{\text{exc}}}{\varepsilon_M}\right)\frac{\overline{\mathbf{r}}\cdot\hat{\boldsymbol{\alpha}}}{|\mathbf{r}|^2} \tag{4}$$

and for the spherical geometry is

$$\Phi_\alpha(\mathbf{r}) = \left(\frac{ed_{\text{exc}}}{(\varepsilon_D + 2\varepsilon_M)/3}\right)\frac{\overline{\mathbf{r}}\cdot\hat{\boldsymbol{\alpha}}}{|\mathbf{r}|^2} \tag{5}$$

We assume that the donor is placed at the origin of the reference system. From here on, that would be the case for all our expressions unless stated otherwise. It is worth mentioning that, for a point-like donor and an exciton in donor QW, the same equation for the electric potential is used because the effective relative permittivity for an exciton in a QW is $\varepsilon_{\text{eff}} = \varepsilon_M$. Therefore, the derivation of the FRET rate, when the donor is a point-like or a QW, will yield the same expression. In the remaining of the article, we will treat these cases as one.

In this paper, we provide the derived analytical expressions for γ_{trans} to study the effects of the background medium relative permittivity and the nanostructure geometries on the FRET rates. We pay particular attention to maximizing the FRET rates between different donor and acceptor pairs while changing the background medium permittivity. We limit our studies to the
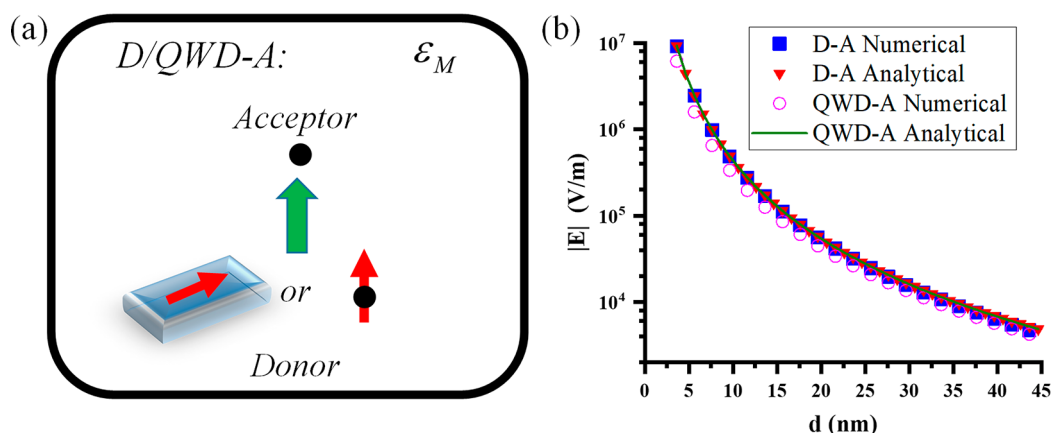
Figure 1. (a) Schematic representation of the D/QWD-A case. (b) Electric field magnitude on the point-like acceptor computed using the analytical expression derived from eq 4 and $\mathbf{E}_\alpha(\mathbf{r}) = -\nabla\Phi_\alpha(\mathbf{r})$ (red triangle dotted line and green line) and via numerical electromagnetic simulations (blue square and circle magenta dotted lines).
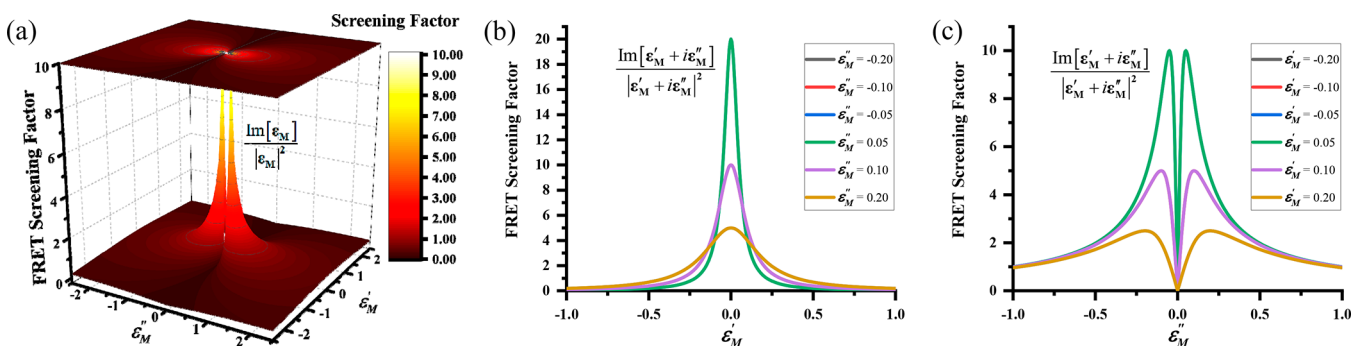

Figure 2. (a) FRET screening factor map as a function of the real and imaginary parts of the background medium permittivity. The plot is truncated at 10 for illustration purposes. FRET screening factor for the selected values $\varepsilon'_M, \varepsilon''_M = \pm\{0.20, 0.10, 0.05\}$ as a function of (b) the real part and (c) the imaginary part of the medium permittivity for a donor−acceptor pair. The curves for the negative permittivity values are symmetric, around the positive permittivity values ∼0 due to the symmetry of the screening factor in eq 6.

materials of (*i*) CdSe, $\varepsilon_{Cdse} = 6.33 + i2.17$, and (*ii*) CdS, $\varepsilon_{Cds} = 5.78 + i0.36$, and focus on QD and QW nanostructures because of their potential practical applications in photovoltaics and LED technologies. The donor and acceptor nanostructure parameters used here are QDD radius of 1.2 nm, QDA radius of 1.4 nm, QWD thickness of 1.2 nm, and QWA thickness of 1.5 nm, with a lateral dimension of 30 nm by 40 nm, and in all cases, the initial surface−surface separation distance, between the donor−acceptor pair, is 1 nm. Moreover, the exciton emission wavelength is assumed to be 550 nm. After deriving the analytical expressions for γ_{trans}, we next discuss the maximum FRET rate occurrence, while the background medium permittivity is swept.

II.1. FRET with ENZ Behavior. The FRET rate for the D/QWD-A case [shown in Figure 1(a)] is obtained using eqs 4 and 2 as

$$\text{D/QWD-A: } \gamma_{\alpha,\text{trans}} = \frac{2}{\hbar} b_\alpha (ed_{exc})^2 \left| \frac{\cos^6(\theta_0)}{d^6} \right| \left| \frac{1}{\varepsilon_M} \right|^2 \text{Im}[\varepsilon_M] \tag{6}$$

where $b_\alpha = \frac{1}{3}, \frac{1}{3}, \frac{4}{3}$ and $\alpha = \{x,y,z\}$, respectively. It is observed that the FRET distance dependency in these cases follows the well-known distance dependency of d^{-6} for the point-like acceptor. Next, we validated the derived expression by computing the electric field intensity, $\mathbf{E}_\alpha(\mathbf{r}) = -\nabla\Phi_\alpha(\mathbf{r})$, on the point-like acceptor generated by the point-like donor in the

vacuum by leveraging the expression in eq 4. The calculated *E*-field values are then compared with those obtained by the electromagnetic simulations performed by COMSOL; an excellent match between the results is observed [Figure 1(b)].

By analyzing eq 6, we observed that the transfer rate can be enhanced by tunning the permittivity of the background medium, where the donor−acceptor pair is embedded. In this case, the FRET rate reaches its maximum as the denominator $\text{Im}[\varepsilon_M]/|\varepsilon_M|^2$ goes to zero, i.e., $|\varepsilon_M| \to 0$ [depicted in Figure 2]. It is worth mentioning that the imaginary part of the medium permittivity must be different from zero to achieve energy transfer between the donor and acceptor. Figure 2(a) presents the 3D plot for the FRET screening factor as the medium permittivity approaches zero. This shows the emergence of two strong peaks as real and imaginary parts of the medium permittivity approach zero.

To analyze the individual effect of real and imaginary parts of the permittivity on the FRET screening factor, we fix one of them and vary the other one. Figure 2 also displays the FRET screening factor values by selecting either the imaginary [in Figure 2(b)] or the real part [in Figure 2(c)] of the medium permittivity. We observe that fixing the imaginary part and tuning the real part [Figure 2(b)] yield better screening compared to the opposite case [Figure 2(c)]. By setting $\varepsilon''_M = \pm0.05$ and sweeping the real part, the screening factor increases 20 times. On the other hand, by selecting $\varepsilon'_M = \pm0.05$ and sweeping the imaginary part, the screening factor boosts 10
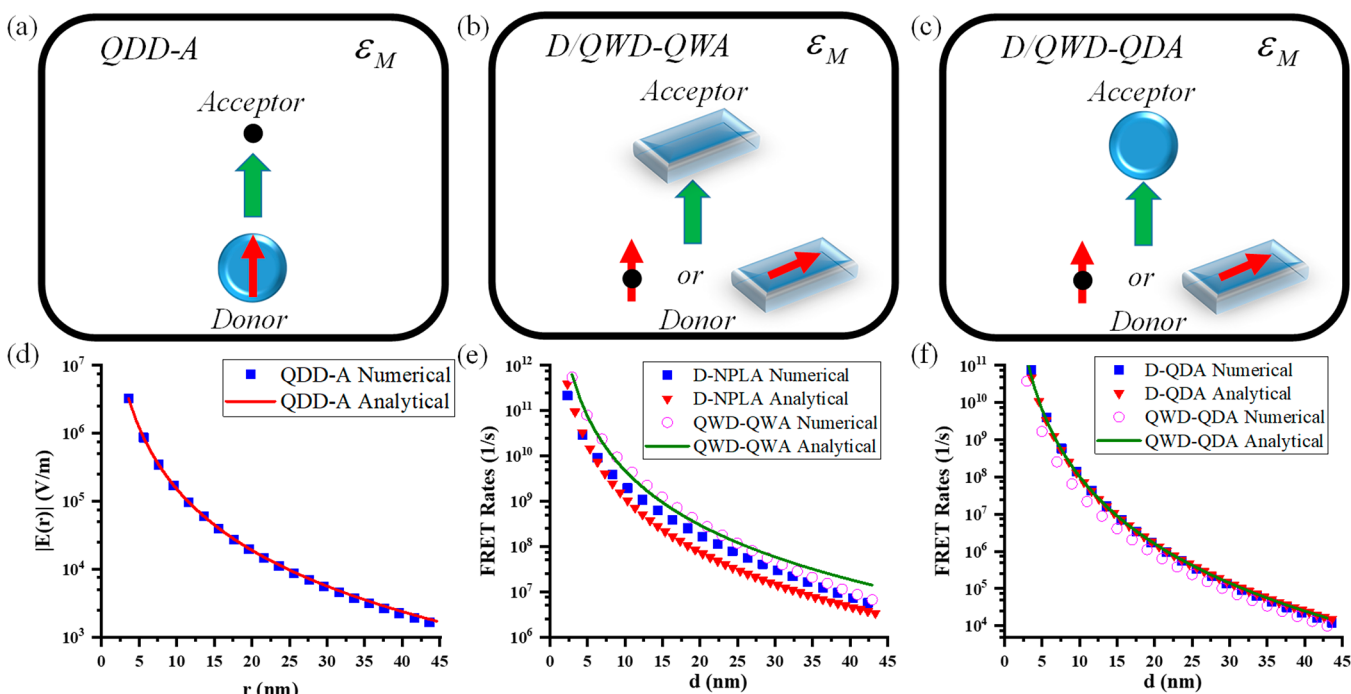
Figure 3. Schematic representation of (a) QDD-A, (b) D/QDD-QWA, and (c) D/QDD-QDA cases. (d) Electric field's magnitude on the point-like acceptor computed using electromagnetic simulations (blue square dotted line) as well as eq 5 and $\mathbf{E}_\alpha(\mathbf{r}) = -\nabla\Phi_\alpha(\mathbf{r})$ (red line) for the QDD-A. FRET rate for the (e) D/QDD-QWA and (f) D/QDD-QDA. Red triangle dotted line and green line represent results from the analytical solution. Blue square and circle magenta dotted lines represent numerical results from numerical simulations. In all cases, we assume that the donor−acceptor pair is embedded in vacuum.

times, half of its counterpart value, due to the FRET rate being proportional to ε_M'' [see Supporting Information Section SII.3(A)]. Hence, manipulating the real part of the permittivity will allow us to tune the screening factor better and consequently increase the FRET rate around the resonance point near zero. It is worth pointing out that for the point-like donor−acceptor pair the FRET screening factor and thus FRET rates have symmetry for the negative and positive regions of the real and imaginary parts of the permittivity, as shown in Figure 2.

II.2. FRET with Single Screening Factor. Next, we increase the complexity of the donor−acceptor particles by analyzing the FRET cases of QDD-A, D/QDD-QWA, and D/QDD-QDA [given in Figure 3(a), (b), and (c), respectively]. By invoking eqs 4, 5, and 2, the FRET rates for these cases are obtained, respectively, as

$$\text{QDD-A: } \gamma_{\alpha,\text{trans}} = \frac{2}{\hbar} b_\alpha (\text{ed}_{\text{exc}})^2 \left| \frac{\cos^6(\theta_0)}{d^6} \right| \left| \frac{3}{\varepsilon_D + 2\varepsilon_M} \right|^2$$
$$\text{Im}[\varepsilon_M] \tag{7}$$

$$\text{D/QWD-QWA: } \gamma_{\alpha,\text{trans}}$$
$$= \frac{2}{\hbar} b_\alpha (\text{ed}_{\text{exc}})^2 \frac{1}{d^4} \left| \frac{2}{\varepsilon_A + \varepsilon_M} \right|^2 \text{Im}[\varepsilon_A] \tag{8}$$

$$\text{D/QWD-QDA: } \gamma_{\alpha,\text{trans}}$$
$$= \frac{2}{\hbar} b_\alpha (\text{ed}_{\text{exc}})^2 R_A^3 \frac{\cos^6(\theta_0)}{d^6} \left| \frac{3}{\varepsilon_A + 2\varepsilon_M} \right|^2 \text{Im}[\varepsilon_A] \tag{9}$$

Here, $b_\alpha = \frac{1}{3}, \frac{1}{3}, \frac{4}{3}$ and $\alpha = \{x,y,z\}$, for the QDs, respectively, and $b_\alpha = \frac{3}{16}, \frac{3}{16}, \frac{3}{8}$ and $\alpha = \{x,y,z\}$, for the QWs, respectively. In eqs 7 and 9, the FRET rate for the spherical case follows d^{-6} distance dependence since the acceptor is a point-like particle and a QD, which has 3D confinement, respectively. In eq 8, the FRET rate for the rectangular case follows d^{-4} distance dependency since the acceptor is subject to 2D confinement. We verified and validated our analytical equations by calculating the electric field intensity, $\mathbf{E}_\alpha(\mathbf{r}) = -\nabla\Phi_\alpha(\mathbf{r})$, at the acceptor side, for the QDD-A [Figure 3(d)], and by calculating the FRET rate for the D/QDD-QWA [Figure 3(e)] and D/QDD-QDA [Figure 3(f)]. We compare the results obtained by the analytical expressions with the ones obtained by numerical simulations. In all cases, we assume that the donor−acceptor pair is embedded in vacuum. As we can observe from the figures, the analytical and numerical results match very well, confirming the validity of the derived analytical expressions.

The FRET rates, in eqs 7, 8, and 9, have a screening factor due to the change in permittivity between the donor/acceptor and the medium. In these configurations, the screening factors change according to the boundary conditions of the donor/acceptor geometry, i.e., rectangular symmetry for a QW and spherical symmetry for a QD. In QW, an exciton "feels" confinement only in one direction compared to the spherical case, which is subject to confinement in three directions. This screening factor can be exploited to improve the energy transfer between the donor and acceptor. The screening factors for a QDD-A, D/QWD-QWA, and D/QWD-QDA cases are 9 Im$[\varepsilon_M]/|\varepsilon_D + 2\varepsilon_M|^2$, 4 Im$[\varepsilon_A]/|\varepsilon_A + 2\varepsilon_M|^2$, and 9 Im$[\varepsilon_A]/|\varepsilon_A + 2\varepsilon_M|^2$, respectively. When the denominators of the screening factors go to zero, i.e., $\varepsilon_D + 2\varepsilon_M \to 0$, $\varepsilon_A + \varepsilon_M \to 0$, and $\varepsilon_A + 2\varepsilon_M \to 0$, respectively, the transfer rates reach their maxima. It is
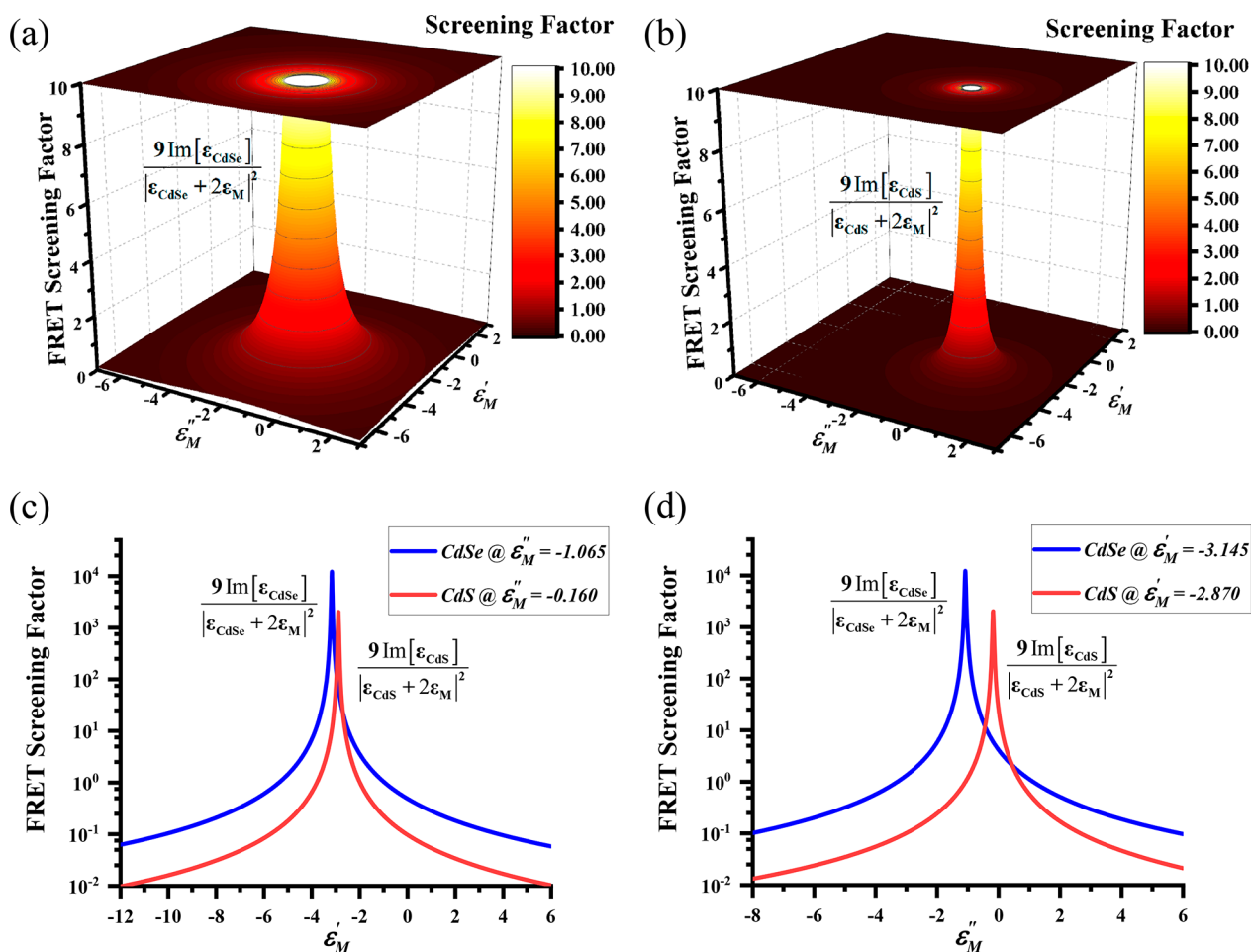
Figure 4. FRET screening factor map as a function of the real and imaginary parts of the medium permittivity for (a) CdSe, $\varepsilon_{CdSe} = 6.33 + i2.17$, and (b) CdS, $\varepsilon_{CdS} = 5.78 + i0.36$. The plots are truncated at the value of 10 for illustration purposes. (c) FRET screening factor for CdSe (blue line, $\varepsilon_M'' = -1.065$) and CdS (red line, $\varepsilon_M'' = -1.060$) as a function of the real part of the medium permittivity. (d) FRET screening factor for CdSe (blue line, $\varepsilon_M' = -3.145$) and CdS (red line, $\varepsilon_M' = -2.870$) as a function of the imaginary part of the medium permittivity.

worth noticing that for the QDD-A case the imaginary part of the medium permittivity needs to be different from zero to achieve an energy transfer between the donor−acceptor pair. Next, we provide the discussion for eqs 7 and 8 [see Supporting Information Section SII.1] and focus on eq 9 in the main text.

Figure 4 depicts the FRET screening factor for D/QWD-QDA made of CdSe [in Figure 4(a)] and CdS [in Figure 4(b)], respectively. The FRET resonance is located at $\varepsilon_M = -0.5\varepsilon_{\{CdSe,CdS\}}$, and the FRET resonance width is proportional to $\varepsilon_M'' = \varepsilon_{\{CdSe,CdS\}}''$ [see Supporting Information SII.3(B)]. Further analysis on the QD acceptor shows that when ε'' is set at $\varepsilon_M'' = -1.065$ and $\varepsilon_M'' = -0.160$, near the singularity for CdSe and CdS, respectively [Figure 4(c)], the FRET screening factor is stronger for CdSe compared to CdS. Likewise, when ε' is fixed to $\varepsilon_M' = -3.145$ and $\varepsilon_M' = -2.870$ [in Figure 4(d)], the FRET screening factor is stronger for CdSe than CdS. For the case of the D/QWD-QWA [see Supporting Information Section SII.1, Figure S2], similar observations can be made for the FRET rate with the difference that the FRET resonance happens at $\varepsilon_M = \varepsilon_{\{CdSe,CdS\}}$. It is worth mentioning that Figure 4 and Figure S2 show single peaks compared to the case of a point-like acceptor in Figure S1. The single FRET peak comes from the fact that FRET is proportional to the imaginary part of the acceptor's permittivity, $Im[\varepsilon_A]$, as compared to the medium's permittivity, $Im[\varepsilon_M]$, in the case of the point-like acceptor.

II.3. FRET with Double Screening Factor. In this section, we consider the cases of QDD-QDA and QDD-QWA [shown in Figures 5(a) and (b)]. Using eqs 4, 5, and 2, the FRET transfer rates for a QD and QW acceptor are obtained, respectively, as

QDD-QDA: $\gamma_{\alpha,trans}$

$$= \frac{2}{\hbar} b_\alpha (ed_{exc})^2 R_A^3 \frac{\cos^6(\theta_0)}{d^6} \left| \left| \frac{3}{\varepsilon_D + 2\varepsilon_M} \right| \right|^2 \left| \frac{3\varepsilon_M}{\varepsilon_A + 2\varepsilon_M} \right|^2$$

$$Im[\varepsilon_A] \qquad (10)$$

QDD-QWA: $\gamma_{\alpha,trans}$

$$= \frac{2}{\hbar} b_\alpha (ed_{exc})^2 \frac{1}{d^4} \left| \left(\frac{3}{\varepsilon_D + 2\varepsilon_M} \right) \left(\frac{2\varepsilon_M}{\varepsilon_A + \varepsilon_M} \right) \right|^2 Im[\varepsilon_A] \qquad (11)$$

where $b_\alpha = \frac{1}{3}, \frac{1}{3}, \frac{4}{3}$ and $\alpha = \{x,y,z\}$, respectively, for the QD, and $b_\alpha = \frac{3}{16}, \frac{3}{16}, \frac{3}{8}$ and $\alpha = \{x,y,z\}$, respectively, for the QW. Here, the FRET rate for the QDD-QDA follows d^{-6} distance dependency since the acceptor has 3D confinement. Likewise, the FRET rate for the QDD-QWA follows d^{-4} distance dependency since the acceptor has 2D confinement. We verified
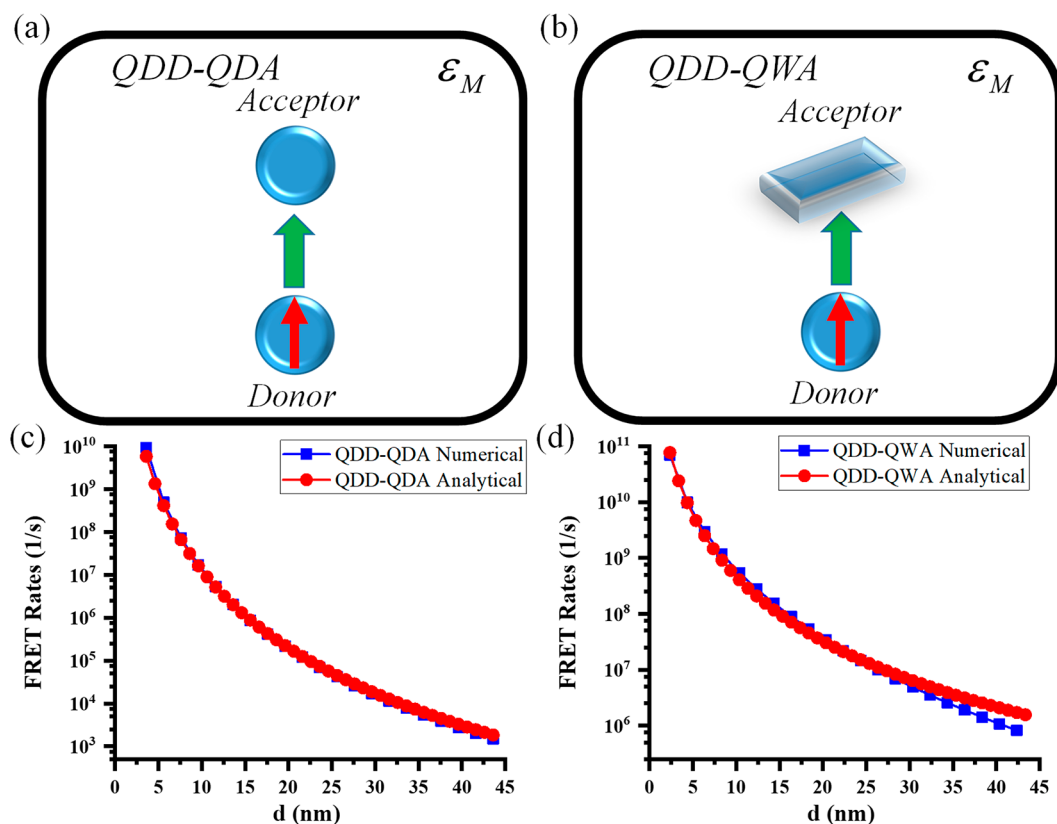
Figure 5. Schematic representations of (a) QDD-QDA and (b) QDD-QWA. FRET rates for (c) QDD-QDA and (d) QDD-QWA cases. Red dotted lines represent results from the analytical solutions, eqs 10 and 11. Blue square dotted lines represent numerical results from numerical electromagnetic simulations. In all cases, we assume that the donor−acceptor pair is embedded in vacuum.

and validated our analytical equations by calculating the FRET rate for the QDD-QDA and the QDD-QWA cases. In both cases, the donor−acceptor pair is assumed to be embedded in a vacuum. Next, we compare the results obtained by eqs 10 and 11 with numerically computed values using electromagnetic software. Figures 5(c) and 5(d) present the FRET rate calculated using both methods. As we can observe, the analytical and numerical results match very well, confirming our analytical expressions.

Similar to the previous section, the transfer rates, eqs 10 and 11, feature a screening factor due to the change in permittivity between the donor and the medium as well as the acceptor and the medium, which can be exploited to enhance the energy transfer between the donor−acceptor pair. In the case of QDD-QDA, the FRET screening factor is given by $\mathrm{Im}[\varepsilon_A](3/|\varepsilon_D + 2\varepsilon_M|)^2 (3\varepsilon_M/|\varepsilon_A + 2\varepsilon_M|)^2$, which exhibits two resonances, one at $\varepsilon_D + 2\varepsilon_M \to 0$ and another one at $\varepsilon_A + 2\varepsilon_M \to 0$, for the FRET rates. Figure 6 depicts the FRET screening factor when the QDD and QDA are made of CdSe [in Figure 6(a)] and CdS [in Figure 6(b)]. As expected, both figures show a single singularity because the donor and acceptor are composed of the same material. However, we can split this resonance into two if we choose two different materials for the donor and the acceptor. For instance, Figure S3 [Supporting Information Section SII.2] plots the FRET screening factor for a CdS QDD and a CdSe QDA. Here, we observe the splitting of the two resonances due to the donor−acceptor pair having different compositions. Further analysis on the medium permittivity, for the single composition of the QDD-QDA pair (CdSe or CdS only) [Figure 6], shows that setting ε_M'' or ε_M' to the resonance values

$(\varepsilon_M'' = -0.5\varepsilon_{\{CdSe,CdS\}}'', \varepsilon_M' = -0.5\varepsilon_{\{CdSe,CdS\}}')$ does not affect much the FRET screening factor, as displayed in Figures 6(c) and 6(d), respectively. Here, we observe a single peak with a maximum value around 10^{10}. Similar behavior is obtained in the case of CdS QDD and CdSe QDA [Figure S3, Supporting Information Section SII.2]; however, the FRET screening factor is smaller on the order of 10^6. Even though the FRET screening factor is several orders of magnitude smaller than the single composition for the QDD-QDA pair, having different materials for the QDD-QDA pair provides an extra degree of freedom since the obtained resonance is wider compared to the case of a single composition. This wider region can be exploited to engineer the resulting benefits of the QDD-QDA pair.

In the case of QDD-QWA, the FRET screening factor, $\mathrm{Im}[\varepsilon_A](3/(|\varepsilon_D + 2\varepsilon_M|)^2(2\varepsilon_M/|\varepsilon_A + \varepsilon_M|)^2$, exhibits two resonances, one at $\varepsilon_D + 2\varepsilon_M \to 0$ and a second one at $\varepsilon_A + 2\varepsilon_M \to 0$, as shown in Figure 7. Even though we use the same material for the donor and the acceptor, we observe two resonances because of the difference in geometry between the QDD and the QWA. These two resonances can be further modified by having different compositions for the QDD and the QWA [see Figure S4, Supporting Information Section SII.2]. Figure 7 depicts the case when the QDD-QWA pair is made of CdSe [Figure 7(a)] and CdS [Figure 7(b)]. In both cases, the resonance's width is shaped by material composition. For instance, CdS has smaller $\varepsilon_{CdS}'' = 0.36$; thus, there is a smaller enhancement between the two resonances than those of CdSe $\varepsilon_{CdSe}'' = 2.17$ [see Supporting Information Section SII.3(C)]. Further analysis on the medium permittivity, for a single composition for the QDD-QWA pair (CdSe or CdS only),
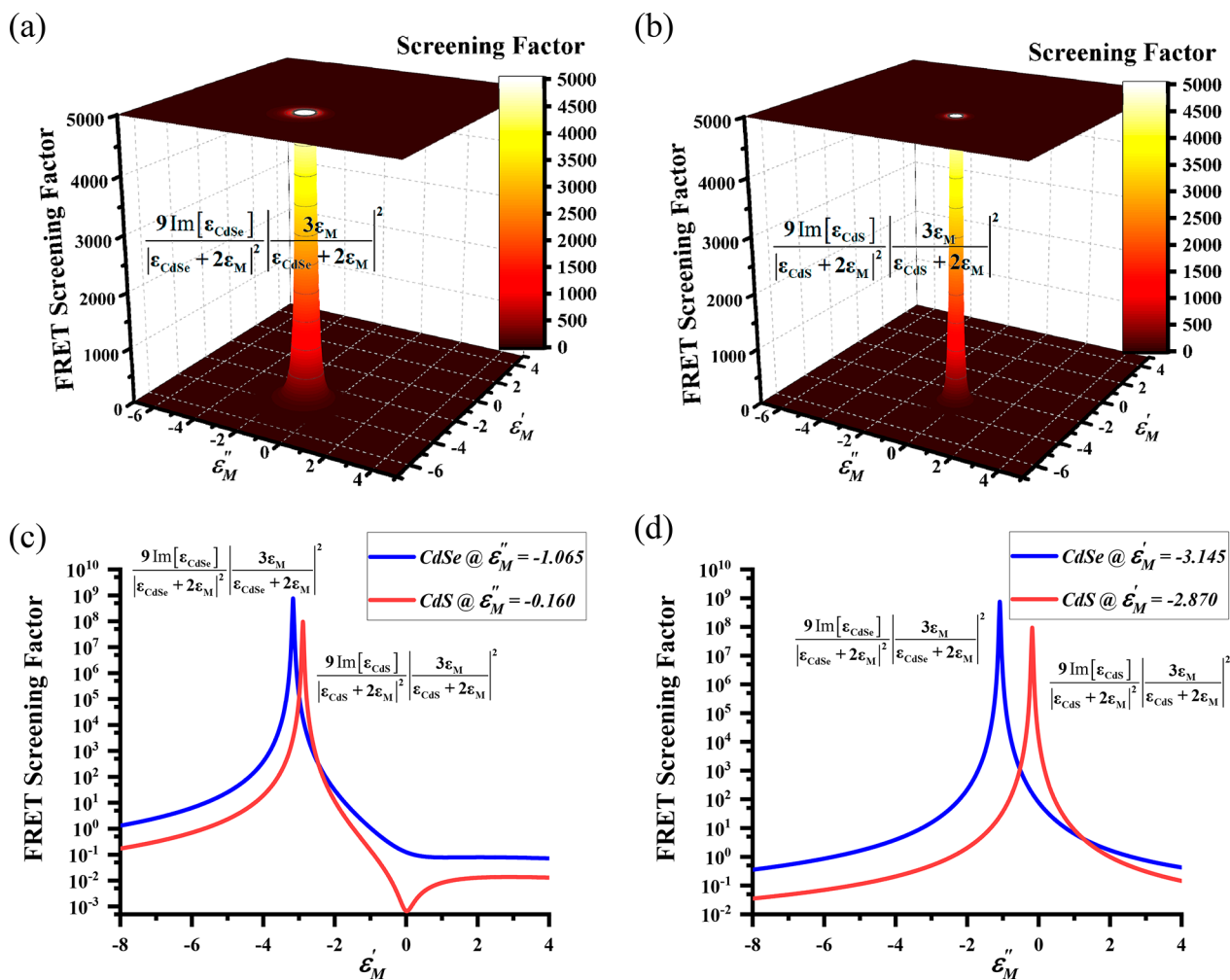
Figure 6. FRET screening factor map as a function of the real and imaginary parts of the medium permittivity for (a) CdSe, $\varepsilon_{CdSe} = 6.33 + i2.17$, and (b) CdS, $\varepsilon_{CdS} = 5.78 + i0.36$. The plots are truncated at the value of 5000 for illustration purposes. (c) FRET screening factor for CdSe (blue line, $\varepsilon''_M = -1.065$) and CdS (red line, $\varepsilon''_M = -0.160$) as a function of the real part of the medium permittivity. (d) FRET screening factor for CdSe (blue line, $\varepsilon'_M = -0.145$) and CdS (red line, $\varepsilon'_M = -2.870$) as a function of the imaginary part of the medium permittivity.

reveals that fixing ε''_M or ε'_M to the resonance values ($\varepsilon''_M = -0.5\varepsilon''_{\{CdSe,CdS\}}$, $\varepsilon'_M = -0.5\varepsilon'_{\{CdSe,CdS\}}$) does not affect much the maximum of FRET screening factor, as shown in Figure 7(c) and Figure 7(d), respectively. However, Figure 7(c) demonstrates that fixing $\varepsilon''_M = -1.065$ and $\varepsilon'_M = -0.160$, near the resonance for CdSe and CdS, yields two peaks, one at $\varepsilon'_M = -0.5\varepsilon'_{\{CdSe,CdS\}}$ and another at $\varepsilon'_M = -\varepsilon'_{\{CdSe,CdS\}}$, respectively. On the other hand, when ε' is set to $\varepsilon'_M = -3.145$ and $\varepsilon'_M = -2.870$, CdSe and CdS resonance [Figure 7(d)], we observe a single peak since we can only pass one resonance at a time. A similar analysis can be undertaken when the QDD is made of CdS, and the QWA is made of CdSe [see Figure S4, Supporting Information Section SII.2]. It is worth mentioning that having different geometries for the QDD-QWA pair provides an extra degree of freedom since the resonance width is modified, giving us the possibility to engineer the FRET behavior of the QDD-QWA pair.

To finalize our study and emphasize the differences in the FRET screening factor between different geometries, we compute the FRET enhancement factor (γ_M/γ_{vacuum}) for the following donor-acceptor pairs: (1) QDD-QDA, (2) QWD-QDA, (3) QDD-QWA, and (4) QWD-QWA. In all cases, the donor-acceptor pair is assumed to be made of CdSe material

($\varepsilon_{D(A)} = 6.33 + i2.17$). Moreover, the fabrication of the desired background medium permittivity can be archived by using the digital metamaterial approach proposed by Engheta et al.,[19] where a digital metamaterial can be synthesized with a targeted complex permittivity by using two elemental materials, with two distinct permittivity functions, as building blocks. Then, we compare the FRET enhancement factor when the donor-acceptor pair is embedded in a medium with $\varepsilon_M = \varepsilon'_M + i$ and compared it against the cases when they are embedded in vacuum. Figure 8 shows the FRET enhancement (γ_M/γ_{vacuum}) for these cases on a semilog scale. We observed that QDD-QDA and QDD-QWA have maximum FRET enhancement factors of 229.3 and 321.5, respectively (blue and red lines, respectively), which are larger compared to the cases of QWD-QDA and QWD-QWA with their corresponding maximum FRET factors of 4.2 and 5.8, respectively (green and magenta lines, respectively). For example, when we choose the medium with relative permittivity $-2 + i$ (purple dot-line), which can be fabricated using, for example, Ag and SiN layers,[18] the FRET rate is boosted 53 times for the QDD-QDA case than using the same nanostructures in the vacuum. Likewise, in the QWD-QDA case, the FRET rate is increased 3 times. On the other hand, for the complementary case (QDD-QWA), the enhance-
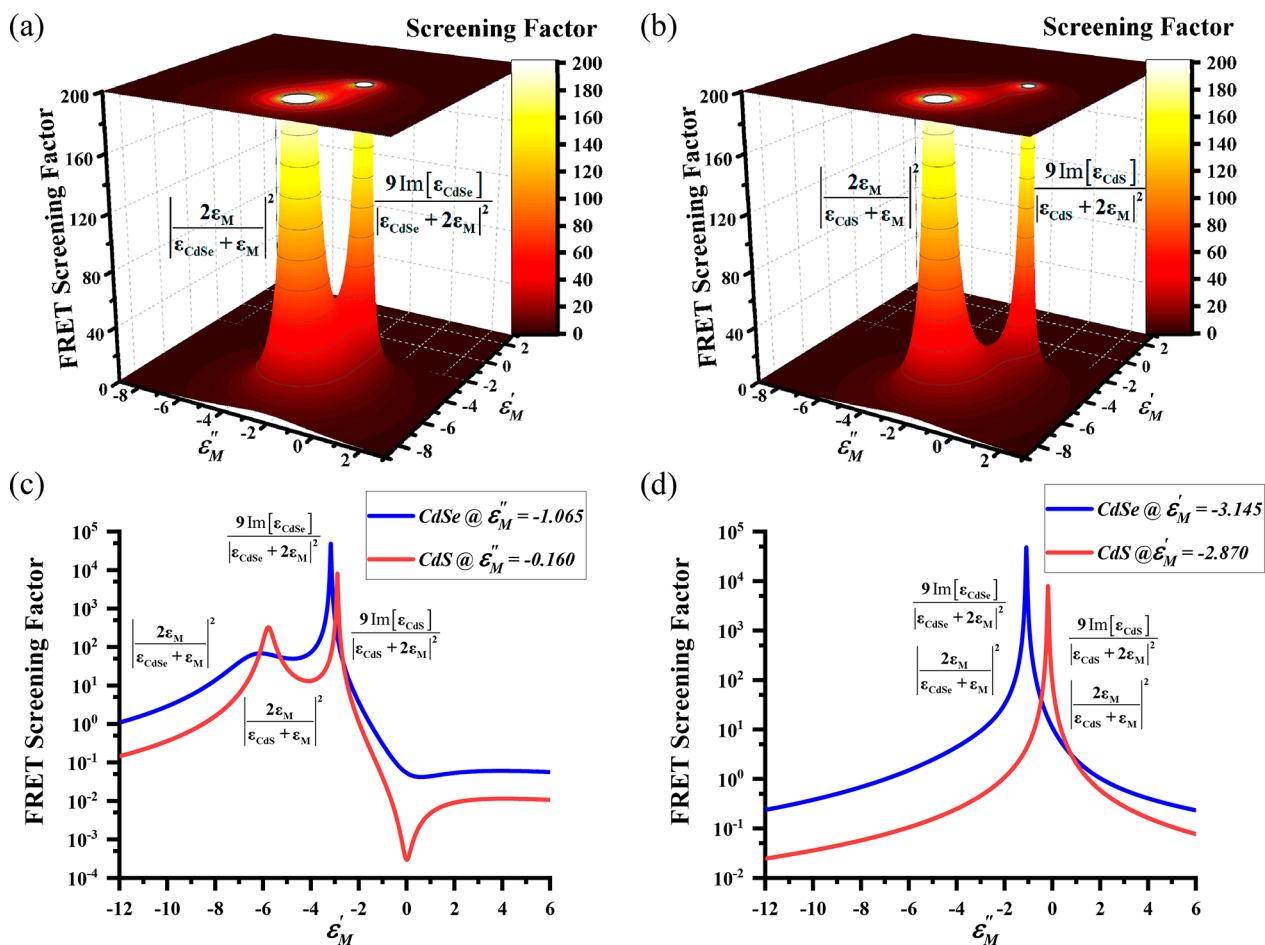
Figure 7. FRET screening factor map as a function of the real and imaginary parts of the medium permittivity for (a) CdSe, $\varepsilon_{CdSe} = 6.33 + i2.17$, and (b) CdS, $\varepsilon_{CdS} = 5.78 + i0.36$. The plots are truncated at the value of 200 for illustration purposes. (c) FRET screening factor for CdSe (blue line, $\varepsilon_M'' = -1.065$) and CdS (red line, $\varepsilon_M'' = -0.160$) as a function of the real part of the medium permittivity. (d) FRET screening factor for CdSe (blue line, $\varepsilon_M' = -3.145$) and CdS (red line, $\varepsilon_M' = -2.870$) as a function of the imaginary part of the medium permittivity.
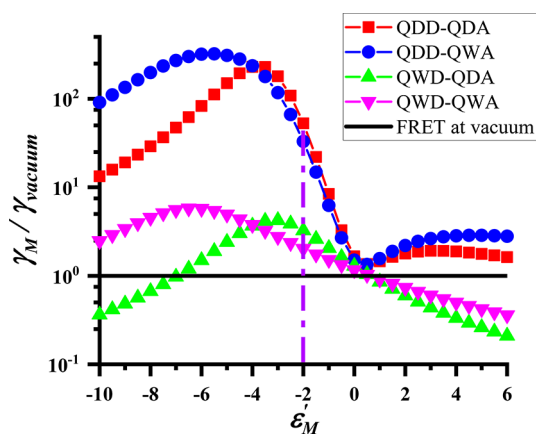

Figure 8. FRET enhancement factor (γ_M/γ_{vacuum}) as a function of the real part of the permittivity of the dielectric medium for the FRET pairs of QDD-QDA, QWD-QDA, QDD-QWA, and QWD-QWA.

ment factor reaches 32 times. Finally, for the QWD-QWA case, the FRET rate can be raised 2 times. Consequently, we observe that the FRET enhancement factor resonance is determined by combining different donor−acceptor pair geometries. These findings suggest that the donor confinement geometry plays a significant role in the FRET enhancement factor. Therefore,

engineering the donor−acceptor pair along with the background permittivity can significantly boost the FRET rates.

III. CONCLUSION

In this work, we showed the effect of the permittivities of the background medium, donor, and acceptor on the FRET rates. Our study revealed that the FRET rate can be substantially enhanced when the screening effects' denominator goes to zero, creating a resonance similar to the plasmonic effect. Each resonance is characterized by the quantum confinement of the donor or acceptor. This property allows us to exploit and tune the resonances according to the application at hand. For example, for a CdSe QDD-QDA pair embedded in a medium with permittivity of $\varepsilon = -2 + i$, the FRET rate can be boosted ∼53-fold compared to that in vacuum. The FRET rate can be further increased up to ∼229 when the permittivity reaches the resonance point at $\varepsilon = -3.7 + i$, for this particular case. Similarly, for the CdSe QWD-QDA case, the resonance occurs at $\varepsilon = -3 + i$, with an enhancement factor of ∼4. On the contrary, in the QDD-QWA case, the enhancement factor reaches ∼321 at $\varepsilon = -5.6 + i$. Finally, for the QWD-QWA pair, the FRET rate can be enhanced 5.8 times at $\varepsilon = -6.2 + i$, compared to that in vacuum. These results suggest that the choice of the donor confinement geometry is essential to reach the desired levels of the FRET enhancement factor. Thus, engineering the donor−acceptor pair

geometries along with the complex permittivity of the background medium can significantly boost the FRET rates. This work shows highly promising practical pathways for enhancing the FRET rate/efficiency and consecutively FRET-based applications including light harvesting (e.g., in photovoltaics), light generation (e.g., in LEDs), light detection (e.g., in photodetectors), and sensing. Currently, our efforts to incorporate such background-enhanced ultraefficient FRET into the system of light emitters are underway.

■ ASSOCIATED CONTENT

ⓈI Supporting Information

The Supporting Information is available free of charge at https://pubs.acs.org/doi/10.1021/acs.jpcc.1c02685.

Further details on Sections II.1, II.2, and II.3 (PDF)

■ AUTHOR INFORMATION

Corresponding Authors

Abdulkadir C. Yucel — LUMINOUS! Center of Excellence for Semiconductor Lighting and Display, School of Electrical and Electronic Engineering, Nanyang Technological University, Singapore 639798, Singapore; Email: acyucel@ntu.edu.sg

Hilmi Volkan Demir — LUMINOUS! Center of Excellence for Semiconductor Lighting and Display, School of Electrical and Electronic Engineering, Nanyang Technological University, Singapore 639798, Singapore; Physics and Applied Physics Division, School of Physical and Mathematical Sciences, Nanyang Technological University, Singapore 639798, Singapore; Department of Physics, Department of Electrical and Electronics Engineering, UNAM - National Nanotechnology Research Center and Institute of Materials Science and Nanotechnology, Bilkent University, Ankara 06800, Turkey; ⓞ orcid.org/0000-0003-1793-112X; Email: hvdemir@ntu.edu.sg

Author

Pedro Ludwig Hernandez-Martinez — LUMINOUS! Center of Excellence for Semiconductor Lighting and Display, School of Electrical and Electronic Engineering, Nanyang Technological University, Singapore 639798, Singapore; Physics and Applied Physics Division, School of Physical and Mathematical Sciences, Nanyang Technological University, Singapore 639798, Singapore; ⓞ orcid.org/0000-0001-6158-0430

Complete contact information is available at:
https://pubs.acs.org/10.1021/acs.jpcc.1c02685

Notes

The authors declare no competing financial interest.

■ ACKNOWLEDGMENTS

■ REFERENCES

(1) Lakowicz, J. R. *Principles of Fluorescence Spectroscopy*; Springer Science+Bussines Media, LLC: New York, 2006.

(2) Hernández-Martínez, P. L.; Govorov, A. O. Exciton Energy Transfer between Nanoparticles and Nanowires. *Phys. Rev. B: Condens. Matter Mater. Phys.* **2008**, 78, 035314/1−035314/7.

(3) Hernández-Martínez, P. L.; Govorov, A. O.; Demir, H. V. Generalized Theory of Förster-Type Nonradiative Energy Transfer in Nanostructures with Mixed Dimensionality. *J. Phys. Chem. C* **2013**, 117, 10203−10212.

(4) Hernández-Martínez, P. L.; Govorov, A. O.; Demir, H. V. Förster-type Nonradiative Energy Transfer for Assemblies of Arrayed Nanostructures: Confinement Dimension vs. Stacking Dimension. *J. Phys. Chem. C* **2014**, 118 (9), 4951−4958.

(5) Taghipour, N.; Hernández-Martínez, P. L.; Ozden, A.; Olutas, M.; Dede, D.; Gungor, K.; Erdem, O.; Perkgoz, N. K.; Demir, H. V. Near-Unity Efficiency Energy Transfer from Colloidal Quantum Wells of CdSe/CdS Nanoplatelets to a Monolayer of MoS_2. *ACS Nano* **2018**, 12, 8547.

(6) Govorov, A. O.; Lee, J.; Kotov, N. A. Theory of Plasmon-Enhanced Förster Energy Transfer in Optically Excited Semiconductor and Metal Nanoparticles. *Phys. Rev. B: Condens. Matter Mater. Phys.* **2007**, 76, 125308/1−125308/16.

(7) Govorov, A. O.; Bryant, G. W.; Zhang, W.; Skeini, T.; Lee, J.; Kotov, N. A.; Slocik, J. M.; Naik, R. R. Exciton-Plasmon Interaction and Hybrid Excitons in Semiconductor-Metal Nanoparticle Assemblies. *Nano Lett.* **2006**, 6, 984−994.

(8) Fedutik, Y.; Temnov, V. V.; Schöps, O.; Woggon, U.; Artemyev, M. V. Exciton-Plasmon-Photon Conversion in Plasmonic Nanostructures. *Phys. Rev. Lett.* **2007**, 99, 136802/1−136802/4.

(9) Su, X.-R.; Zhang, W.; Zhou, L.; Peng, X.-N.; Wang, Q.-Q. Plasmon-Enhanced Förster Energy Transfer Between Semiconductor Quantum Dots: Multipole Effects. *Opt. Express* **2010**, 18, 6516−6521.

(10) Ziolkowski, R. W. Propagation in and Scattering from a Matched Metamaterial having a Zero Index of Refraction. *Phys. Rev. E* **2004**, 70, 046608.

(11) Silveirinha, M. G.; Engheta, N. Tunneling of Electromagnetic Energy through Subwavelength Channels and Bends using ε-Near-Zero Materials. *Phys. Rev. Lett.* **2006**, 97, 157403.

(12) Enoch, S.; Tayeb, G.; Sabouroux, P.; Guérin, N.; Vincent, P. A Metamaterial for Directive Emission. *Phys. Rev. Lett.* **2002**, 89, 213902.

(13) Alù, A.; Silveirinha, M. G.; Salandrino, A.; Engheta, N. Epsilon-Near-Zero Metamaterials and Electromagnetic Sources: Tailoring the Radiation Phase Pattern. *Phys. Rev. B: Condens. Matter Mater. Phys.* **2007**, 75, 155410.

(14) Caspani, L.; Kaipurath, R. P. M.; Clerici, M.; Ferrera, M.; Roger, T.; Kim, J.; Kinsey, N.; Pietrzyk, M.; Di Falco, A.; Shalaev, V. M.; et al. Enhanced Nonlinear Refractive Index in n-Near-Zero Materials. *Phys. Rev. Lett.* **2016**, 116, 233901.

(15) Poddubny, A. N.; Belov, P. A.; Kivshar, Y. S. Purcell Effect in Wire Metamaterials. *Phys. Rev. B: Condens. Matter Mater. Phys.* **2013**, 87, 035136.

(16) Chebykin, A. V.; Orlov, A. A.; Shalin, A. S.; Poddubny, A. N.; Belov, P. A. Strong Purcell Effect in Anisotropic n-Near-Zero Metamaterials. *Phys. Rev. B: Condens. Matter Mater. Phys.* **2015**, 91, 205126.

(17) Jacob, Z.; Smolyaninov, I. I.; Narimanov, E. E. Broadband Purcell Effect: Radiative Decay Engineering with Metamaterials. *Appl. Phys. Lett.* **2012**, 100, 181105.

(18) Maas, R.; Parsons, J.; Engheta, N.; Polman, A. Experimental Realization of an Epsilon-Near-Zero Metamaterial at Visible Wavelengths. *Nat. Photonics* **2013**, 7, 907−912.

(19) Della Giovampaola, C.; Engheta, N. Digital metamaterials. *Nat. Mater.* **2014**, 13, 1115−1121.